European Journal of Nuclear Medicine and Molecular Imaging (2025) 52:2628–2644
https://doi.org/10.1007/s00259-025-07074-9

ORIGINAL ARTICLE

Protein-functionalized and intrinsically radiolabeled [^{188}Re]ReO_x nanoparticles: advancing cancer therapy through concurrent radio-photothermal effects

Sanchita Ghosh[1,2] · Apurav Guleria[2,3] · Sourav Patra[1,2] · Avik Chakraborty[2,4] · Kanhu Charan Barick[2,5] · Chandan Kumar[1,2] · Khajan Singh[1] · Sutapa Rakshit[4] · Rubel Chakravarty[1,2]

Received: 26 July 2024 / Accepted: 30 December 2024 / Published online: 25 January 2025

Abstract

Purpose Enhancing therapeutic effectiveness is crucial for translating anticancer nanomedicines from laboratory to clinical settings. In this study, we have developed radioactive rhenium oxide nanoparticles encapsulated in human serum albumin ([^{188}Re]ReO_x-HSA NPs) for concurrent radiotherapy (RT) and photothermal therapy (PTT), aiming to optimize treatment outcomes.

Methods [^{188}Re]ReO_x-HSA NPs were synthesized by a controlled reduction of $^{188}ReO_4^-$ in HSA medium and extensively characterized. The anticancer effect of [^{188}Re]ReO_x-HSA NPs was demonstrated in vitro in murine melanoma (B16F10) cell line. In vivo SPECT/CT imaging, autoradiography and biodistribution studies were performed after intratumoral injection of [^{188}Re]ReO_x-HSA NPs in melanoma tumor-bearing C57BL/6 mice. The potential of [^{188}Re]ReO_x-HSA NPs for combined RT and PTT treatment was also demonstrated in the aforesaid mice model.

Results [^{188}Re]ReO_x-HSA NPs (size 4–6 nm) were synthesized with high colloidal and radiochemical stability. Upon laser (808 nm) exposure on B16F10 cells incubated with [^{188}Re]ReO_x-HSA NPs, only < 20% of cells were alive demonstrating high therapeutic efficacy under in vitro settings. Uniform dose distribution and retention of the radiolabeled NPs in the tumor volume were observed via SPECT/CT imaging and autoradiography studies. Tumor growth in mice model was significantly arrested with ~ 1.85 MBq dose of [^{188}Re]ReO_x-HSA NPs and simultaneous laser irradiation, demonstrating synergistic benefit of RT and PTT.

Conclusions These results demonstrate that intrinsically radiolabeled [^{188}Re]ReO_x-HSA NPs having unique features such as high photothermal effects and favorable nuclear decay characteristics for combined RT/PTT, hold great promise for clinical translation.

✉ Rubel Chakravarty
rubelc@barc.gov.in; rubelchakravarty@gmail.com

1 Radiopharmaceuticals Division, Bhabha Atomic Research Centre, Trombay, Mumbai 400085, India

2 Homi Bhabha National Institute, Anushaktinagar, Mumbai 400094, India

3 Radiation and Photochemistry Division, Bhabha Atomic Research Centre, Trombay, Mumbai 400085, India

4 Radiation Medicine Centre, Bhabha Atomic Research Centre, Parel, Mumbai 400012, India

5 Chemistry Division, Bhabha Atomic Research Centre, Trombay, Mumbai 400085, India

Graphical Abstract

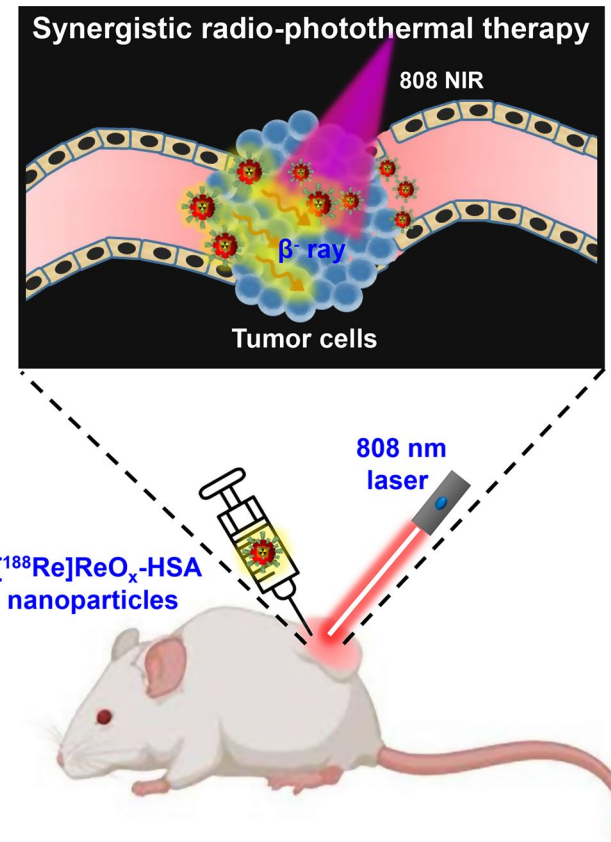

Keywords ^{188}Re · Combination therapy · CT contrast · Intrinsically radiolabeled · Photothermal therapy · Radiotherapy · Theranostics

Introduction

Despite significant advancements in medical science, cancer remains a major cause of death globally. The GLOBOCAN 2024 report indicated approximately 20 million new cases of cancer and 9.7 million cancer-related deaths occurred worldwide in the year 2022 alone [1]. Hence, it is imperative to take immediate steps to enhance research endeavors aimed at creating efficient methods for the early detection, monitoring, and treatment of cancer. Nanomedicine represents a promising frontier in the battle against cancer, leveraging advancements to enhance early detection and treatment strategies [2–7]. NPs can be engineered to target specific biomarkers or molecular signatures associated with cancer cells, enabling early detection even at the molecular level [8, 9]. This precision enhances the likelihood of detecting cancer in its earliest and most treatable stages, potentially improving patient outcomes and survival rates. NPs can also deliver therapeutic agents directly to cancer cells, minimizing damage to healthy tissues and reducing the systemic toxicity often associated with conventional therapeutic modalities [10–13].

Recently, combination therapies using functionalized NPs in cancer treatment have become increasingly promising by harnessing synergistic effects to improve therapeutic efficacy and overcome resistance mechanisms [14, 15]. One particularly impactful approach involves combining RT with PTT for enhanced therapeutic efficacy [16, 17]. RT utilizes ionizing radiation to induce DNA damage and cell death within the tumor, while PTT employs specific materials to convert near-infrared (NIR) light into heat, selectively ablating cancer cells through localized hyperthermia [16, 17]. The integration of RT and PTT offers several complementary advantages. While RT has long been employed in clinical settings, certain cancers develop resistance to it because of their distinct tumor hypoxic microenvironments [18, 19]. In such cases, PTT can augment the effects of RT by increasing tumor oxygenation and sensitizing cancer cells to radiation-induced damage. Moreover, PTT can target residual or radioresistant cancer cells that survive RT,

thereby potentially reducing recurrence rates and improving long-term outcomes. Furthermore, this combination therapy approach minimizes systemic toxicity compared to traditional chemotherapy, as both RT and PTT primarily target localized tumor sites. This strategy holds significant promise in enhancing treatment efficacy, reducing side effects, and potentially improving overall survival rates for cancer patients.

Rhenium oxide and other transition-metal oxides are notable for their ability to exhibit strong localized surface plasmon resonance (LSPR) in the near-infrared (NIR) region due to their unique outer valence electron configurations [20, 21]. They specifically demonstrate metallic conductivity at temperatures below 500 K and exhibit exceptionally high LSPR absorbance, comparable to that of gold [20, 21]. Hence it is possible to utilize rhenium oxide as a promising photothermal agent, leveraging its high LSPR absorbance for targeted cancer therapies that require precise and efficient heat generation within tissues [22]. Furthermore, rhenium is a transition metal having an atomic number of 75 making it a promising choice for computed tomography (CT) contrast agent [23]. Additionally, rhenium-188 (^{188}Re) is a well-known therapeutic radionuclide due to its advantageous nuclear decay characteristics [24]. Its therapeutic impact primarily arises from β^- radiation with an energy of 2.1 MeV. Moreover, the 155 keV gamma ray serves practical purposes such as dosimetry and monitoring distribution through single photon emission computed tomography (SPECT) imaging [24]. The rapid radiotherapeutic response of ^{188}Re is facilitated by its short half-life of 16.9 h, distinguishing it from other therapeutic radionuclides. Therefore, radioactive rhenium oxide NPs can serve as an advanced theranostic agent for dual-modality (SPECT/CT) imaging agent and concurrent RT/PTT towards improving cancer management.

Herein, we report the synthesis of human serum album (HSA) encapsulated and intrinsically radiolabeled rhenium oxide NPs ([^{188}Re]ReO_x-HSA NPs) for concurrent RT and PTT (Fig. 1). The radiolabeled nanoformulation was intratumorally administered in melanoma (B16F10) tumor bearing mice followed by illumination with 808 nm laser for PTT. Combined therapy showed significantly higher therapeutic efficacy with minimal side effects on the liver, kidneys, and other organs compared to single-modality therapy. To the best of our knowledge, this is the first report on synthesis of biocompatible and intrinsically radiolabeled noble metal-based nanoagent for dual-modality (SPECT/CT) imaging and concurrent RT/PTT of cancer in preclinical settings.

Experimental

Materials

All chemicals were purchased from Sigma Aldrich (India) if not mentioned otherwise. Albumin from human serum (HSA) was procured from Sigma Life Science, India. Enriched tungsten oxide (99.9% in ^{186}W) was purchased from Isoflex, Russia. Milli-Q water from Milli-Q® Direct Water Purification System (Merck, India) was used for preparation of all the solutions. 0.22 µm Millex-GP syringe filter and PD-10 columns were purchased from Merck-Millipore (India) and G.E. Healthcare (Germany), respectively.

Synthesis and characterization of ReO_x-HSA NPs

In order to prepare HSA coated ReO_x NPs, 20 mg ammonium perrhenate (NH_4ReO_4) and 25 mg HSA were added into 5 mL of water and mixed. Then, 1 mL of 1 M $NaBH_4$ solution was added and vigorously stirred for another 2 h in

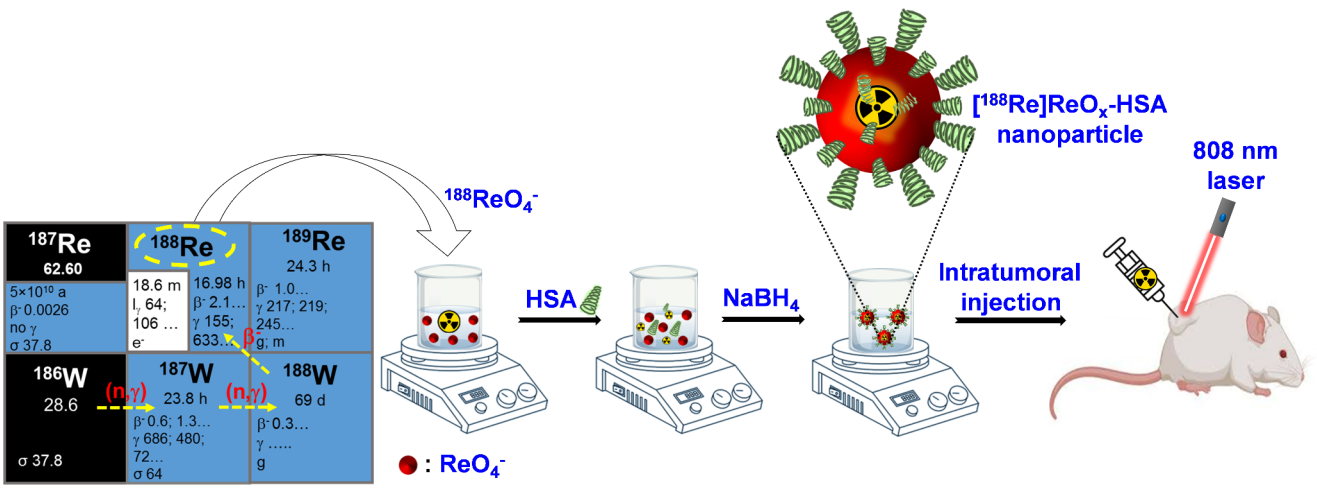

Fig. 1 Schematic representation of [^{188}Re]ReO_x-HSA NPs synthesis

an ice bath. After the stirring the color of the solution turned to dark brown conforming the formation of NPs.

Hydrodynamic diameter of the NPs was measured by employing dynamic light scattering (DLS) technique using Microtrac Series MN420 – Nanotrac Wave II particle analyzer, Germany. To confirm the formation of the NPs, UV-Visible absorption spectra was recorded using a UV-Vis spectrophotometer (JASCO, Japan). High-resolution transmission electron microscopy (HRTEM) images of the NPs were obtained using a Field Emission Gun-Transmission Electron Microscope − 120/200 kV (JEM 2100 F model, JEOL, USA) system. X-ray diffraction (XRD) pattern of the powdered NPs, obtained from Martin Christ lyophilizer (Germany), was recorded using Phillips PW1710 diffractometer. Raman spectral analysis of the NPs was carried out by Seki's STR300 Raman spectrometer. Moreover, the bonding mode of the NPs was studied by X-ray photoelectron spectroscopy (Staib Instruments, Germany). To investigate the amount of coating of HSA on the surface of the NPs thermogravimetric analysis (TGA) was carried out using Mettler Toledo TG/DSC STARe system in inert condition (nitrogen gas flow rate ~ 50 $mL \cdot min^{-1}$) up to 900 °C temperature. To investigate the colloidal stability and the relaxation time of ReO_x-HSA NPs, Xigo Nanotools Acorn Area instrument was used.

Photothermal effect of ReO_x-HSA NPs

In this study, 2 mL of ReO_x-HSA NPs solution of different concentrations (0.25 $mg.mL^{-1}$ – 1 $mg.mL^{-1}$) were taken in a quartz cuvette and illuminated with 808 nm laser (808-LM-2000T) at various power ranging from 0.81 W to 1.0 W with an exposure diameter 0.6 cm for 5 min. The distance between the quartz cuvette and the laser was maintained at 2 cm. To record the temperature change at different time points a fiber optic signal conditioner (FOTEMP1-H, Micronor Inc., US) was utilized. Thermal images of the NPs solution were also captured using Testo 865 – Thermal Imager. Deionized water was taken as a control.

Synthesis of radiolabeled [^{188}Re]ReO_x-HSA NPs

The HSA coated and intrinsically radiolabeled NPs was synthesized by following the similar method as the synthesis of nonradioactive NPs, except the addition of $^{188}ReO_4^-$ in addition to NH_4ReO_4 solution. [^{188}Re]ReO_x-HSA NPs was purified by passing the nanoformulation through a PD-10 column preconditioned with phosphate buffer saline (PBS). The column was eluted with 0.5 mL of PBS and the activity of aliquots was measured in a NaI (Tl) scintillation detector (Mucha, Raytest). The radiochemical stability of [^{188}Re]ReO_x-HSA NPs was evaluated by incubating the purified NPs in 10 times excess volume of PBS and mouse serum.

In vitro studies in cell lines

B16F10 cell line was purchased from National Center for Cell Sciences (NCCS) Pune, India. The cell line was cultured in Dulbecco's modified Eagle medium (DMEM) supplemented with 10% serum (GIBCO), antibiotic/antimycotic solution and 2 mM L-glutamine in a humidified incubator with 5% CO_2 atmosphere at 37 °C.

The cytotoxicity of ReO_x-HSA NPs against B16F10 cells was evaluated by 3-[4,5-dimethylthiazol-2-yl]-2,5 diphenyl tetrazolium bromide (MTT) assay. Briefly, the B16F10 cells were seeded in a 96 well plate (1×10^3/well) and incubated with various concentration of ReO_x-HSA NPs. After 24 h, the cell culture medium was replaced with 10 µL (5 mg mL^{-1}) MTT reagent and was incubated again for 4 h at 37 °C. The formed formazan crystal was solubilized by addition of 100 µL solubilizing buffer (20% SDS in 50% DMF). Then the absorbance of formazan was measured at 570 nm using BioTek Universal Microplate reader. The percentage of cell viability was calculated using (optical density of treated cells/ optical density of control cells) x 100 formula.

For assessment of PTT, RT and combined RT/PTT effects under in vitro conditions, B16F10 cells were seeded in a 96 well plate. Among them, one set of cells were incubated with 0.5 mg mL^{-1} ReO_x-HSA NPs for 12 h, second set of cells were incubated with 0.5 mg mL^{-1} ReO_x-HSA NPs for 12 h and irradiated with 808 nm laser at 0.81 W for 5 min, third set of cells were incubated with only [^{188}Re]ReO_x-HSA NPs (185 kBq mL^{-1}) for 12 h and fourth set of cells were incubated with [^{188}Re]ReO_x-HSA NPs (185 kBq mL^{-1}) for 12 h followed by irradiation with 808 nm laser at 0.81 W for 5 min. Standard MTT assay was carried out to determine the relative cell viability after 24 h of treatment.

CT contrast imaging with ReO_x-HSA NPs

In order to evaluate the computed tomography (CT) contrast property of ReO_x-HSA NPs, 200 µL of NPs solution having different concentration range (0–6 mg mL^{-1}) were placed in a 96 well plate and images were recorded using a GE SPECT/CT system, 670DR, USA.

All animal experiments were carried out by following the regulations approved by Institutional Animal Ethics Committee of Bhabha Atomic Research Centre. Approximately, 2×10^6 B16F10 melanoma cells suspended in PBS were subcutaneously injected into the left shoulder of C57BL/6 mice. The melanoma tumor bearing mice were used for imaging when the tumor diameter reached 6–8 mm. CT images of the tumor bearing animal anesthetized with isoflurane were

recorded before and 24 h after intratumoral injection of 4.5 mg mL^{-1} ReO_x-HSA NPs.

SPECT/CT imaging, tumor autoradiography and biodistribution studies using [^{188}Re]ReO_x-HSA NPs

Melanoma tumor bearing mice were intratumorally injected with the radiolabeled NPs (50 µL, ~ 18.5 MBq) diluted in PBS and SPECT/CT images were recorded after 1, 24, 48 h post injection (p.i.) in a GE SPECT/CT imaging system (Model: 670DR), USA. To assess the homogeneous distribution of radiolabeled NPs, another group of tumor bearing mice were intratumorally injected with 50 µL [^{188}Re]ReO_x-HSA NPs (~9.3 MBq) and after 24 h p.i. they were euthanized by carbon dioxide. Afterwards, the tumor tissue slice was cut and kept between autoradiographic plates for 24 h and image of autoradiographic plate was captured using camera. Moreover, to quantitatively estimate the uptake of the NPs in different organs, 9.3 MBq dose of [^{188}Re]ReO_x-HSA NPs was intratumorally injected in tumor bearing mice and the mice were sacrificed at different time points (1 h, 24 h, 48 h, 72 h) p.i. by asphyxiation with carbon dioxide. Using a NaI(Tl) detector, percentage of radioactivity accumulated in different organs and blood were detected and reported as percent of injected dose per gram (%ID/g) [25].

Therapy studies

To evaluate the therapeutic efficacy of [^{188}Re]ReO_x-HSA NPs, the mice with melanoma tumor were randomly divided into different groups having 4 animals in each group. Only PTT was carried out in the following manner: mice group treated with (i) 0.5 mg mL^{-1} of ReO_x-HSA NPs and 808 nm laser irradiation after 1 day p.i.; (ii) 0.5 mg mL^{-1} of ReO_x-HSA NPs and 808 nm laser irradiation after 1st and 4th day p.i.; (III) 0.5 mg mL^{-1} of ReO_x-HSA NPs and 808 nm laser irradiation after 1st, 4th and 8th day p.i. All photothermal experiments were carried out at 0.81 W power for 5 min. RT was conducted in different mice groups which were injected with (i) 0.5 MBq of [^{188}Re]ReO_x-HSA NPs; (ii) 0.9 MBq of [^{188}Re]ReO_x-HSA NPs; (iii) 1.85 MBq of [^{188}Re]ReO_x-HSA NPs; (iv) 2.78 MBq of [^{188}Re]ReO_x-HSA NPs; (v) 3.7 MBq of [^{188}Re]ReO_x-HSA NPs. To evaluate the combined effect from RT and PTT, another group of mice was intratumorally injected with 1.85 MBq of [^{188}Re]ReO_x-HSA NPs followed by 808 nm laser (at 0.81 W power) irradiation for 5 min at (i) 1 day p.i.; (ii) 1st and 4th day p.i. and (iii) 1st, 4th and 8th day p.i. As a control, normal saline was also injected in one group of mice. All the mice were observed for 16 days while recording the tumor volume and the body weight of the mice. Tumor growth index (TGI) and body weight index (BWI) were calculated by the standard formula [26]. Tumor and other important organs (i.e. kidney, liver, lungs) were harvested of the group (control) treated with saline and the group treated with 1.85 MBq of [^{188}Re]ReO_x-HSA NPs followed by 808 nm laser irradiation at 1st and 4th day p.i. for histopathological analysis according to a standard procedure [27]. Biochemical and hematological parameters of blood samples were also analyzed for treated and non-treated mice [28].

Results

Synthesis and characterization of ReO_x-HSA NPs

HSA coated rhenium oxide NPs were synthesized by controlled reduction of NH_4ReO_4 with $NaBH_4$. Figure 2a & b shows the HRTEM images of the HSA coated ReO_x NPs. Few more images have been provided as supporting information (Figure S1). The as observed agglomeration of NPs in most of the TEM images can be attributed to the presence of protein on their surface, prompting self-assembling. The lattice fringes as well as the selected area electron diffraction (SAED) ring pattern (inset of Fig. 2a) signify the polycrystalline nature of the NPs. Further, the NPs were found to be quasi-spherical (or pseudo-spherical) with an average size ranging between 4 and 6 nm. The as determined average size is in well-agreement with that obtained from the DLS studies, i.e., 15.6 ± 0.8 nm (Fig. 2c). DLS gives information about the hydrodynamic size, while TEM measures actual average size of particles. So, it is expected that the average size determined from the DLS studies would be higher than TEM measurements. Moreover, the hydrodynamic diameter of the NPs did not change significantly over a period of 7 days (Figure S2). T_2 relaxation time of the ReO_x-HSA NPs (Figure S3) also validated the conclusions drawn from DLS studies. T_2 relaxation time of the freshly prepared NPs was 2874 ± 28 ms, which decreased to 2737 ± 23 ms after a period of 10 days. This negligible change in T_2 relaxation time showed that as synthesized NPs retained their colloidal stability over a period of at least 10 days.

Nonetheless, the as observed predominantly quasi-spherical shape of the NPs might be correlated to the plausible changes in the conformation of protein coating their surface. To examine this possibility, circular dichroism (CD) spectra of the solutions of HSA and HSA coated ReO_x NPs were recorded to analyze any changes in the protein structure during the formation of NPs, as can be seen from Figure S4. For this purpose, the pH values of the solutions of HSA and HSA coated ReO_x NPs were adjusted to match with each other. The pH of the colloidal solution of HSA was determined to be ~5.0. And, it is well-known that the α-helical structure of HSA is conserved between pH 5.0 to 10.0 [29]. It can

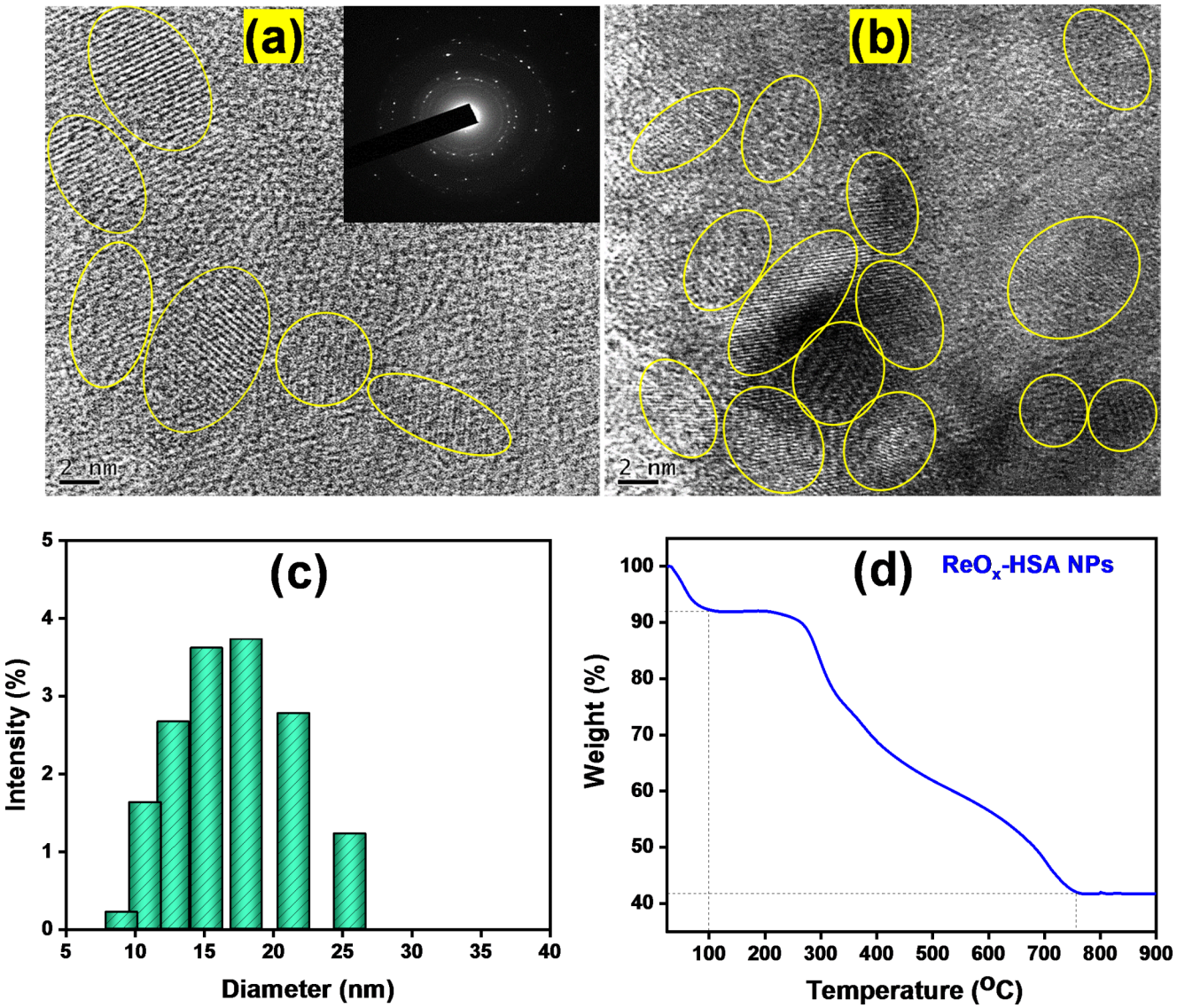

Fig. 2 HRTEM images (**a** & **b**) of HSA coated ReO_x NPs. The inset of image (**a**) shows the SAED pattern of the NPs. (**c**) Size distribution plot from DLS. (**d**) TGA analysis of ReO_x-HSA NPs

be seen that HSA at pH 5.0 exhibits two negative bands at 209 and 222 nm, which essentially arise from the n → π* transition for the peptide bond of α-helix structure of the protein [29]. In the presence of Re precursor and subsequent formation of HSA coated ReO_x NPs, the pH of the solution was determined to be 8.0. Interestingly, the solution of HSA coated ReO_x NPs shows dramatic decrease of intensity of both of these bands of HSA without any shift in the band maxima. Moreover, the CD spectral profile of the solution of HSA at pH 8.0 and HSA coated ReO_x NPs were found to match with little variations in the band intensities. Nonetheless, CD spectral studies indicate conformational changes of HSA coating the ReO_x NPs with decrease in its α-helix content. Moreover, in the recent times, it has been reported by various researchers that the protein conformation induced by pH could drastically affect the morphology of the NPs [30, 31].

UV-Visible absorption spectra of HSA coated ReO_x NPs is shown in Figure S5. The spectral profile of HSA and Re precursor i.e., ammonium perrhenate is also shown in the absorption plot. As can be seen, no significant absorption could be observed beyond 300 nm in case of ammonium perrhenate and HSA. A characteristic peak of HSA at 278 nm can be observed, which is generally associated with its aromatic amino acids (tryptophan and tyrosine residues). While, the colloidal solution of HSA coated ReO_x NPs exhibited considerable absorption in the region ranging from 300 to 500 nm along with the HSA peak at 278 nm. The appearance of such feature signifies the formation of ReO_x NPs. Similar absorption spectral features have been

reported by Anantharaj et al. in their study on the synthesis of ultra-small ReO_x NPs immobilized on DNA scaffolds [32].

XRD analysis of the NPs was also carried out to confirm the structure of the NPs. The broad featureless XRD pattern of the ReO_x-HSA NPs ascertains its formation and suggests robust coating of HSA on the surface (Figure S6). The weight% coating of HSA on the NPs surface was calculated from TGA analysis, displayed in Fig. 2d. The weight loss at 100 °C was due to the free water molecules present on the NPs surface and the subsequent weight loss is related to the HSA coating on the NPs surface. Nearly 50% of HSA was coated on the inorganic ReO_x core.

Raman spectra of HSA and HSA coated ReO_x NPs have been shown in the Figure S7. To have a better understanding of the interactions involved, the Raman spectrum of rhenium precursor, i.e., ammonium perrhenate is also provided in the Figure S7. The peaks in the Raman spectrum of HSA can be categorized into 3 groups, i.e., amide-I band (1600 to 1700 cm^{-1}), amide-II band (1480 to 1600 cm^{-1}) and amide-III band (1220 to 1330 cm^{-1}) [33, 34]. The vibrational modes represented by amide-I band originate primarily from C═O stretching. The amide-II band is mainly attributed to N–H bending with a contribution from C–N stretching vibrations, while amide-III can be assigned to the C–N stretching mode coupled to the in-plane N–H bending mode. It can be seen from the Raman spectra that the HSA vibrational peaks of amide-I, II and III bands disappeared in case of ReO_x-HSA NPs. In addition to that, some other peaks of HSA such as tyrosine doublet (~828 and 850 cm^{-1}) were not observed in the Raman spectrum of ReO_x-HSA NPs. However, some vibrational peaks of HSA such as 505 cm^{-1} (ν (S–S)), 642 (ν (C–S)), 896 cm^{-1} (ring vibrations of aromatic amino acids), 935 cm^{-1} (ν (C–C)) and 1000 cm^{-1} (ring vibration of phenylalanine and tryptophan) appeared in the Raman spectrum of ReO_x-HSA NPs, although with less intensity or slight shift [35]. Apart from these, the ammonium perrhenate peaks were observed at 343, 891, 913 and 966 cm^{-1}. The peak at 345 cm^{-1} correspond to the bending mode of ReO_4^-, while peaks at 891, 913 and 966 cm^{-1} can be attributed to its stretching mode [36]. In the Raman spectrum of ReO_x-HSA NPs, ammonium perrhenate peaks were observed with some shift at 337, 922 and 965 cm^{-1}. The well-resolved peak of perrhenate at 891 cm^{-1} could not be observed in the Raman spectrum of ReO_x-HSA NPs. The appearance of a new peak at ~257 cm^{-1} in case of ReO_x-HSA NPs is not precisely clear, however taking into account of the previous reports, it may be assigned to the rotatory (or vibrational) lattice modes of the ammonium ion in ammonium perrhenate [36–38]. Nonetheless, the significant variations in the vibrational peaks (in term of intensity, shift, broadening) of perrhenate anion and the protein in the Raman spectrum of ReO_x-HSA NPs may be attributed to the strong bonding interactions between them (perrhenate anion and HSA) during the formation of NPs.

The composition of the as prepared NPs was further examined by XPS studies. Figure S8 shows the survey spectrum of the NPs, while core level XPS spectra of Re 4f and O 1s are provided in Fig. 3a and b, respectively.

The Re 4f XPS core level spectrum exhibited three peaks centered at 42.2, 45.9 and 48.0 eV. This signifies the presence of Re (in NPs) with multiple oxidation states. Deconvolution resulted in the appearance of four peaks centered at 42.2, 44.5, 46.0, and 48.2 eV. The latter two peaks at 46.0

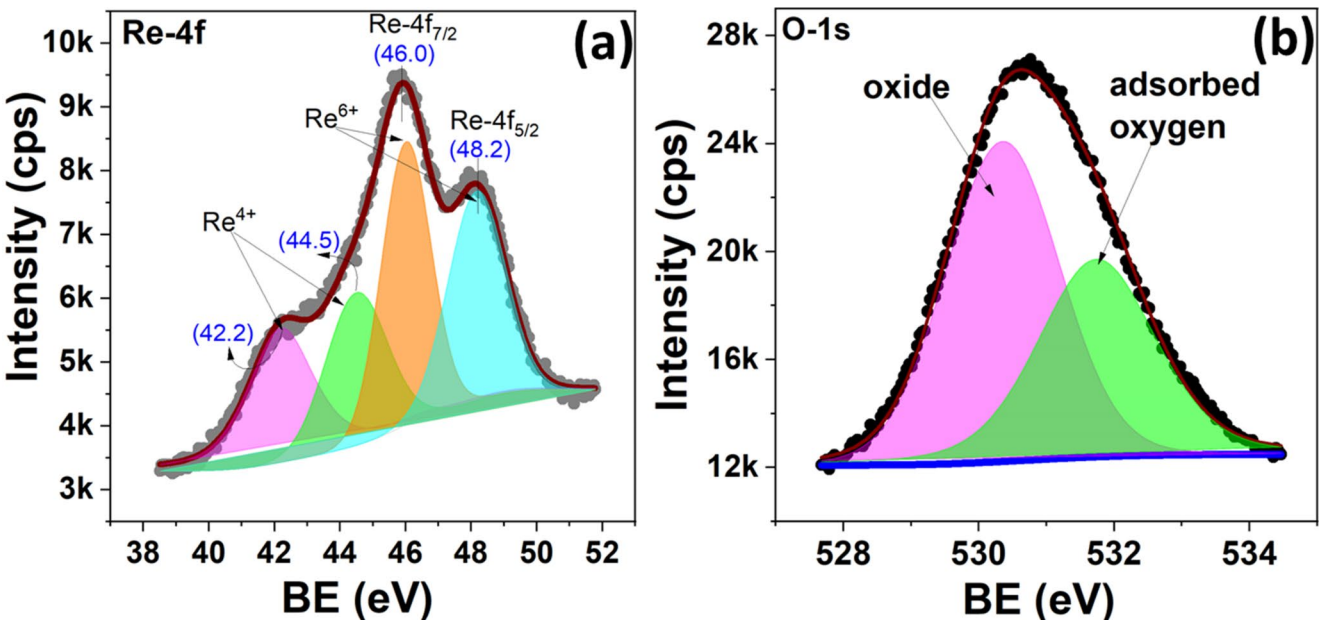

Fig. 3 Core level XPS spectra of Re 4f (**a**) and O 1s (**b**) in HSA coated ReO_x NPs

and 48.2 eV may be attributed to the Re^{6+} 4 $f_{7/2}$ and Re^{6+} 4 $f_{5/2}$, respectively [39, 40]. While, lower binding energy peaks at 42.2 and 44.5 eV may be assigned to the Re^{4+} species [39, 41, 42]. The susceptibility of Re towards oxidation is well-known, as can also be observed from these findings. Further, the O 1s core level spectrum shows the appearance of a broad peak centered at 530.6 eV, which on deconvolution resulted in two peaks at 530.4 and 531.7 eV. As expected, the former peak signifies the formation of oxide, while the latter one may be attributed to the adsorbed oxygen [43, 44].

Photothermal effect of ReO_x-HSA NPs

It has been already discussed in UV-vis spectral analysis that ReO_x-HSA NPs exhibits considerable amount of absorbance in 300 to 500 nm range which implies that the NPs possess good photoactivity. The photothermal performance of the ReO_x-HSA NPs was evaluated by irradiating different concentration (0.25, 0.5, 1 mg mL^{-1}) of the NPs with an 808 nm laser at power 0.81 W and as a control deionized water was used. As depicted in Fig. 4a, the temperature of the NPs increased rapidly only after irradiation of 5 min and the values of temperature change were 12, 19, 28 °C for 0.25, 0.5, 1 mg mL^{-1} of ReO_x-HSA NPs, respectively. Hence, the photothermal effect is concentration dependent in nature. On the contrary, the temperature of deionized water increased only by 2.3 °C. Additionally, the power dependence performance of 0.5 mg mL^{-1} of ReO_x-HSA NPs revealed that at 0.81 W power, the temperature of the NPs could reach up to 48 °C, as shown in Fig. 4b. The observation is also supported by the thermal images, shown in Fig. 4d. These observations indicated that ReO_x-HSA NPs could rapidly convert NIR light energy into thermal energy. Moreover, after 5 cycles of irradiation and cooling, no significant change was visible in the temperature curve (Fig. 4c) which implied good photothermal stability of the NPs.

Synthesis and quality control of [^{188}Re]ReO_x-HSA NPs

The intrinsically radiolabeled [^{188}Re]ReO_x-HSA NPs was synthesized in a similar procedure as described for the non-radioactive NPs synthesis, except the addition of $^{188}ReO_4^-$ (740 MBq) to the nonradioactive ammonium perrhenate solution. Elution of ^{188}Re from an indigenously developed $^{188}W/^{188}Re$ generator and quality control of ^{188}Re are given in detail in the supporting information (**Figures S9 and S10**). Size exclusion chromatographic technique using PD-10 column was utilized to determine the radiochemical purity of the radiolabeled NPs. The NPs formulation was eluted with

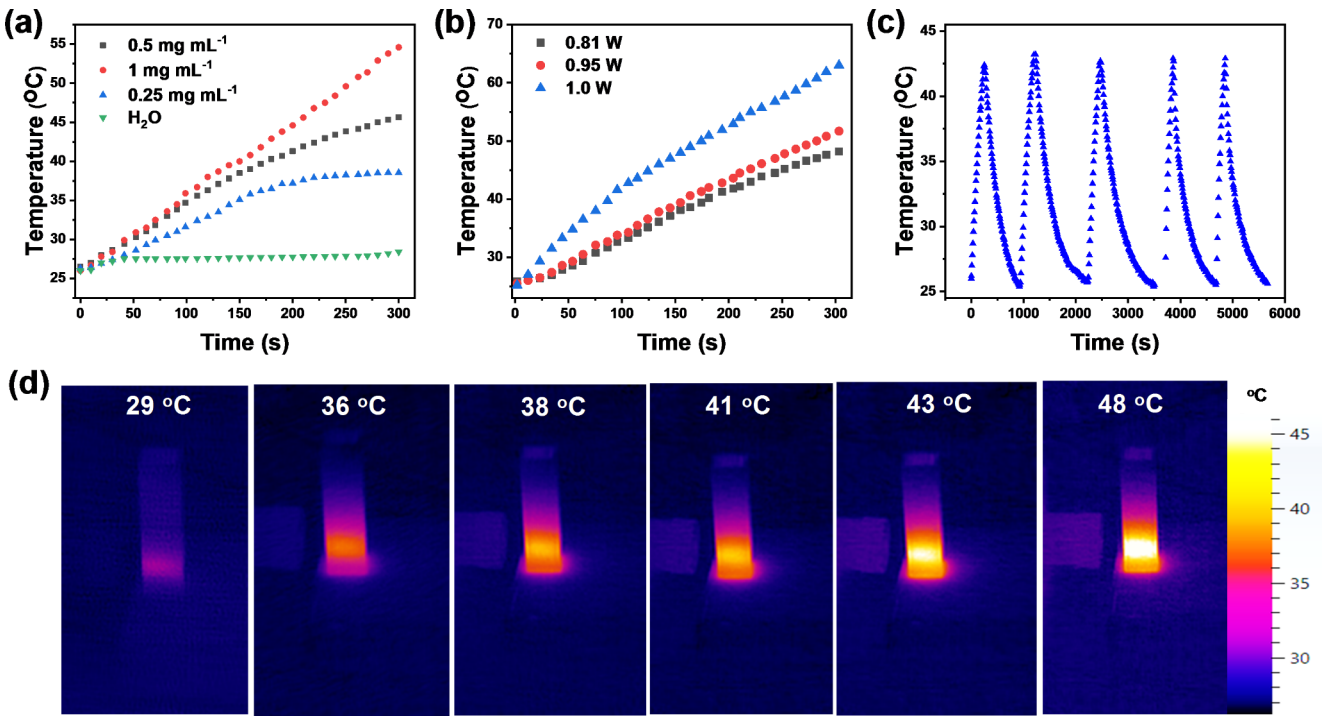

Fig. 4 (**a**) Concentration dependent photothermal curves of ReO_x-HSA NPs and water under irradiation of 808 nm laser at power 0.81 W. (**b**) Power dependent photothermal curves of 0.5 mg mL^{-1} ReO_x-HSA NPs. (**c**) Cycle of in vitro photothermal stability of ReO_x-HSA NPs at power 0.81 W. (**d**) Thermal images of 0.5 mg mL^{-1} ReO_x-HSA NPs under irradiation of 808 nm laser at power 0.81 W at different time points

PBS and nearly 82 ± 3% (n = 3) activity was obtained in 3 to 4 mL fraction (Figure S11a). The radiochemical purity of the radiolabeled nanoformulation obtained in the aforementioned fraction was also determined to be 95 ± 2% after 24 h (Figure S11b). Furthermore radiochemical stability of [^{188}Re]ReO_x-HSA NPs was evaluated in PBS and mouse serum media at 37 °C. After 48 h of observation, 92.3 ± 0.5% (n = 3) of [^{188}Re]ReO_x-HSA NPs was stable in PBS medium (Figure S12a) and in mouse serum medium radiochemical stability was 91.4 ± 0.3% (n = 3) (Figure S12b).

In vitro studies in cell lines

A standard MTT assay was carried out to evaluate the cytotoxic effect of HSA encapsulated ReO_x-HSA NPs by incubating various concentration of NPs in B16F10 cell lines. Even at 500 µg mL^{-1} concentration of NPs, minimal cytotoxicity was found (Fig. 5a). Nearly 91 ± 2% (n = 3) cells were alive when 500 µg mL^{-1} ReO_x-HSA NPs were incubated which suggests biocompatible nature of the NPs in vitro.

Prior to combined RT/PTT, individual treatment modality was performed in by incubating B16F10 cells with ReO_x-HSA NPs and [^{188}Re]ReO_x-HSA NPs, separately. Next, the combined RT/PTT was studied with [^{188}Re]ReO_x-HSA NPs. It was observed that 37 ± 3% (n = 3) cancer cells were destroyed by RT alone ([^{188}Re]ReO_x-HSA NPs, without laser) and PTT (ReO_x-HSA NPs, with laser) destroyed 30 ± 3% (n = 3) cells. On the contrary, combined RT/PTT ([^{188}Re]ReO_x-HSA NPs, with laser) substantially enhanced the therapeutic efficacy by killing 87 ± 2% (n = 3) cells, as shown in Fig. 5b. Additionally, the evaluation by Valeriote's formula also exhibited that the efficacy of the combined RT and PTT was synergistic in nature and was apparently stronger than any single modality treatment (Table S1, Supplementary information) [45].

CT contrast imaging with ReO_x-HSA NPs

High atomic number of Re (Z = 75) makes HSA encapsulated ReO_x NPs as a CT contrast agent [46]. Although numerous high Z metal containing NPs have been proposed in the past, their biocompatibility limits their application for cancer theranostics [47, 48]. Hence, biocompatible ReO_x-HSA NPs has more potential as a CT contrast agent. As shown in Fig. 6a, the attenuation of the NPs increased with the increase in concentration.

To further demonstrate the CT contrast property of the ReO_x-HSA NPs, in vivo CT images were recorded. After intratumoral injection of 4.5 mg mL^{-1} of the NPs in a melanoma tumor bearing mice, excellent tumor contrast (marked by red dotted line) was shown while no contrast signal was found before injecting the NPs in similar condition (Fig. 6b).

SPECT/CT imaging, tumor autoradiography and biodistribution studies using [^{188}Re]ReO_x-HSA NPs

A series of SPECT/CT images of melanoma tumor bearing C57BL/6 mice were recorded at different time intervals after intratumoral injection of [^{188}Re]ReO_x-HSA NPs. The SPECT images clearly demonstrate that the injected NPs remained at the tumor site even after 48 h of administration (Fig. 7a). Furthermore, there was minimal leakage of radioactivity from the tumor site as evident by negligible uptake in other healthy organs (Fig. 7a). The autoradiography of the tumor slice was also carried out by slicing the tumor

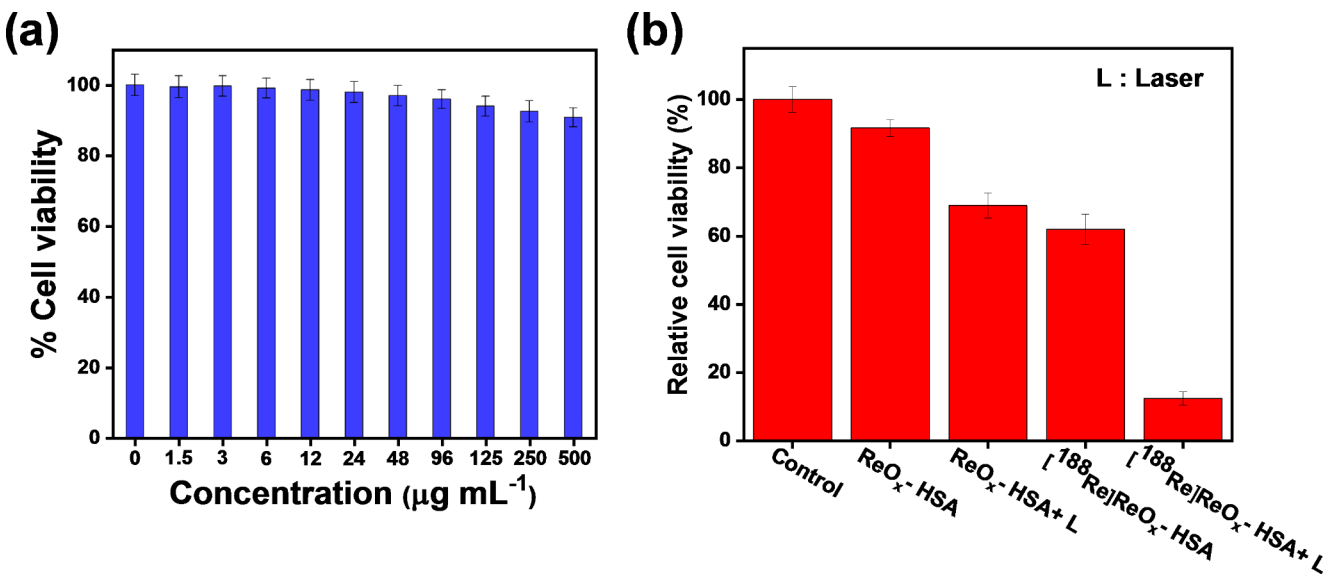

Fig. 5 (**a**) The percentage of cell proliferation of B16F10 cell lines after 24 h incubation with different concentration of ReO_x-HSA NPs. (**b**) The in vitro combination therapeutic effect of PTT and RT along with single modality of treatment in B16F10 cell lines

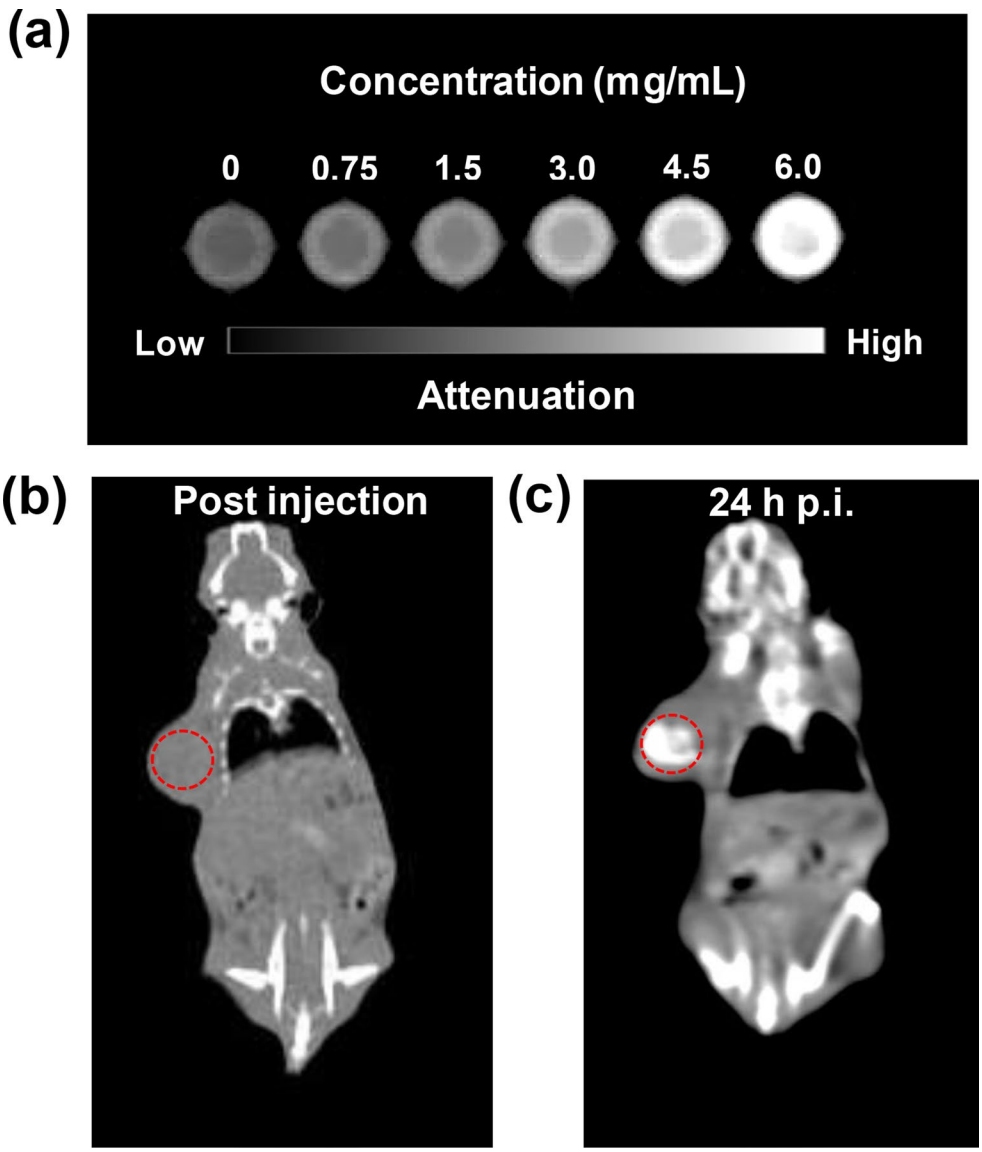

Fig. 6 (**a**) In vitro CT images of ReO_x-HSA NPs dispersion at different concentrations. In vivo CT images of melanoma tumor bearing C57BL/6 mice (**b**) pre and (**c**) post intratumoral injection of ReO_x-HSA NPs. The red circle indicates the position of the tumor

tissue after intratumoral injection of the protein encapsulated radioactive NPs. As shown in Fig. 7b, nearly uniform distribution throughout the tumor of the radiolabeled NPs was achieved. The homogeneous distribution of the NPs is expected to enhance the therapeutic efficacy. Ex vivo biodistribution studies were also conducted after intratumoral injection of [^{188}Re]ReO_x-HSA NPs in melanoma tumor bearing mice, shown in Fig. 7c. The tumor uptake of the NPs was 459.4 ± 23.4%ID/g after 1 h of injection, which was retained significantly even after 72 h p.i. The liver uptake of the radiolabeled NPs increases from 0.7 ± 0.2%ID/g (1 h p.i.) to 1.9 ± 0.4%ID/g (24 h p.i.) and gradually decreases to 0.8 ± 0.1%ID/g at 72 h p.i. The clearance pattern of the NPs indicated that it cleared through hepatobiliary route. Additionally, negligible uptake in other tissues or organs indicated robust in vivo stability of the NPs.

Therapy studies

To evaluate the photothermal ablation property of ReO_x-HSA NPs, the melanoma tumor of C57BL/6 mice were irradiated with 808 nm laser for one (1st day p.i.), two (1st and 4th day p.i.), and three (1st, 4th and 8th day p.i.) times, for 5 min each after intratumoral administration of the NPs. Although tumor growth was arrested significantly for the group treated with two and three-times laser irradiation (Figure S13a), no significant change in BWI was observed (Figure S13b). On the other hand, RT was evaluated by injecting different doses (0.5 MBq, 0.9 MBq, 1.85 MBq, 2.78 MBq and 3.7 MBq) of [^{188}Re]ReO_x-HSA NPs. After 16 days of observation, tumor volume decreased significantly for the groups treated with 2.78 MBq and 3.7 MBq (Figure S14a) but the BWI reduced drastically indicating radiotoxicity effects in the animals (Figure S14b). However,

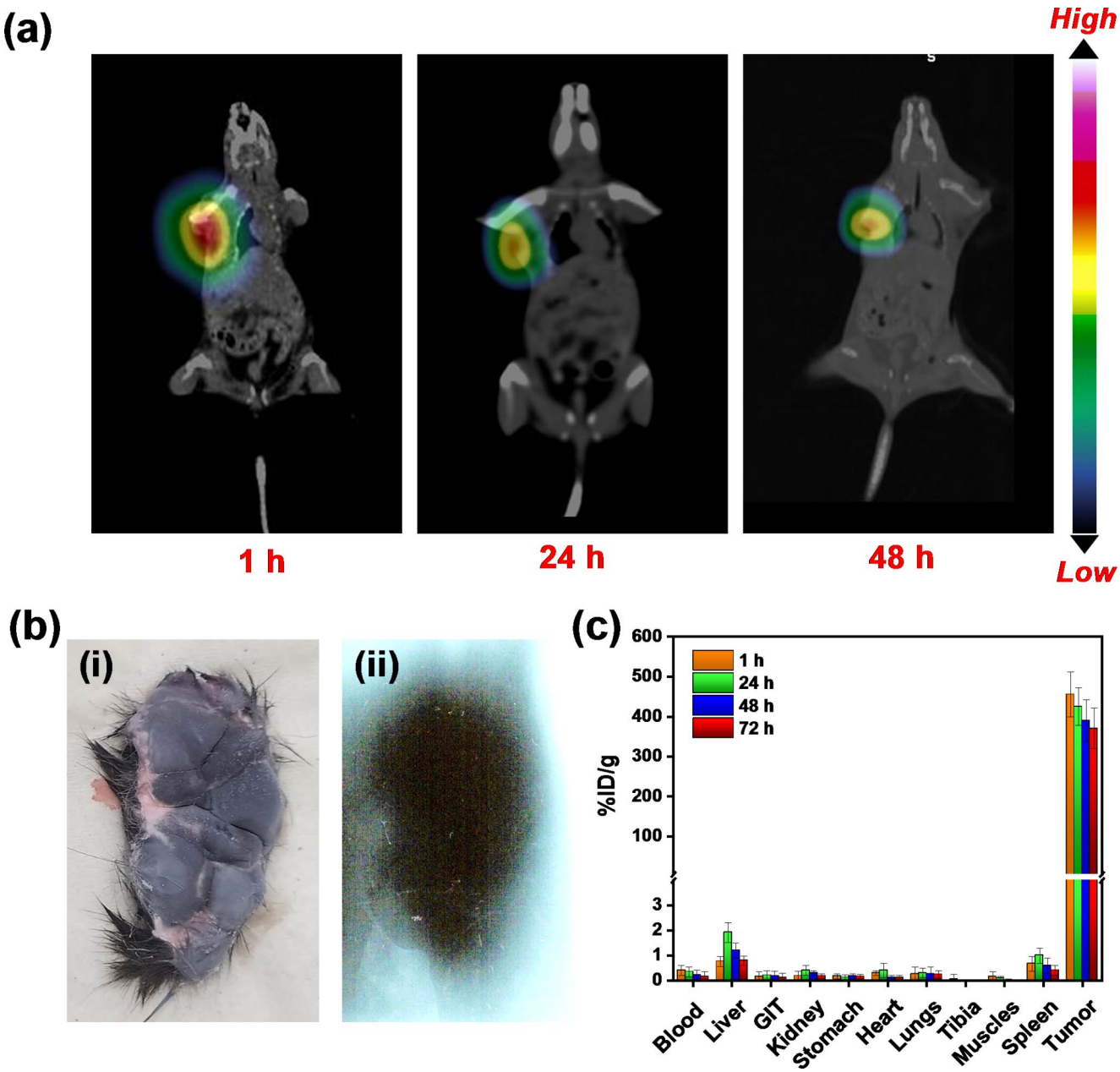

Fig. 7 (**a**) SPECT/CT images of melanoma tumor bearing mouse after intratumoral injection of [^{188}Re]ReO$_x$-HSA NPs at different time points. (**b**) i: B16F10 tumor slice; ii: autoradiography of tumor slice for evaluation of uniform distribution of [^{188}Re]ReO$_x$-HSA NPs after intratumoral injection. (**c**) Ex vivo biodistribution studies of melanoma tumor bearing C57BL/6 mice after intratumoral administration of [^{188}Re]ReO$_x$-HSA NPs ($n=4$)

negligible change in BWI was observed when treated with 1.85 MBq even though appreciable retardation in tumor growth was observed. Based on the observations from RT and PTT studies, synergistic effect of [^{188}Re]ReO$_x$-HSA NPs was evaluated by employing 1.85 MBq dose of radiolabeled NPs followed by one, two and three-time irradiation with 808 nm laser. As shown in Fig. 8a and b, tumor growth was arrested for group treated with both two and three times of irradiation along with RT without significant change in BWI. Depending on these observations, single dose of 1.85 MBq of [^{188}Re]ReO$_x$-HSA NPs along with two times of irradiation with 808 nm laser was the optimal protocol for the combined RT/PTT. No significant changes in biochemical and hematological parameters were observed for the animals treated with RT/PTT compared to healthy mice (Table S2 and Table S3 in supporting information). Histopathological examination was also conducted on critical organs such as the kidney, lungs, liver, and tumor tissue of melanoma tumor bearing C57BL/6 mice treated under the optimal therapeutic procedure along with the nontreated tumor

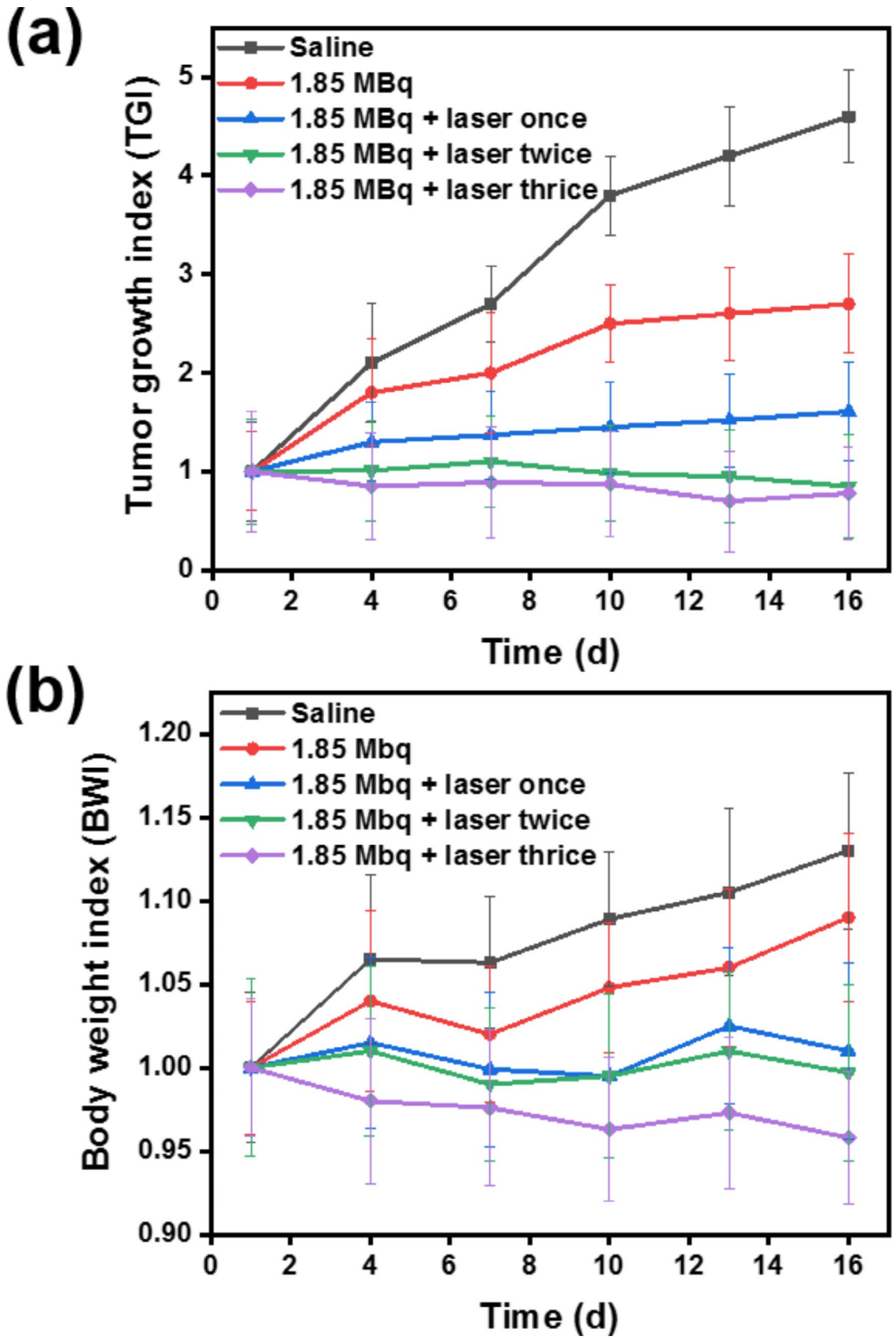

Fig. 8 (a) Tumor growth index ($n=4$) and (b) body weight index ($n=4$) plots of C57BL/6 mice bearing melanoma tumor in different treatments groups

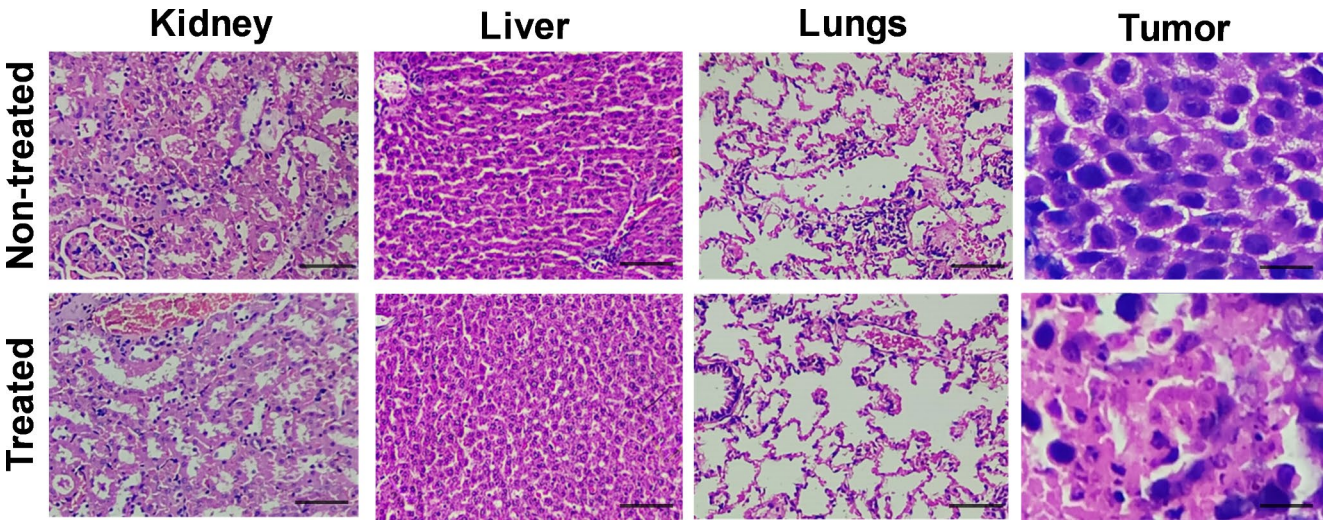

Fig. 9 Hematoxylin and eosin-stained images of kidney, liver, lungs, tumor of non-treated and treated mice with combined RT/PTT. Scale bar = 50 µm

bearing mice (Fig. 9). Comparing the tissue morphology of kidney, liver and lungs between treated animals and non-treated revealed no noteworthy differences were observed. However, conspicuous damage and a reduction in mitotic cells were observed in the tumor tissue of the treated animal groups demonstrating the therapeutic efficacy of [^{188}Re]ReO_x-HSA NPs.

Discussion

The latest developments in nanotechnology have shown the importance of functionalized inorganic NPs as advanced agents for use in cancer theranostic [49]. Such materials possess unique physicochemical properties and can be functionalized with diverse ligands for targeting various types of cancers [49]. To date, several inorganic nanoplatforms have been developed for imaging and therapeutic purposes and their applicability has been demonstrated mostly in preclinical settings [50, 51]. From the perspective of clinical translation, it is desirable that the administered NPs should not only be biocompatible but also show biodegradable characteristics under in vivo conditions to alleviate the concerns related to toxicity. In this premise, Re NPs particularly hold translatable importance as they are reported to get easily oxidized after exposure to oxygen which is an indication of their potential for biodegradation [52]. The typical oxidation product of Re NPs are ReO_4^- ions, which are known to be biocompatible [52]. Therefore, exploring the biomedical application of this class of nanomaterial is presently a hot topic of research [53–57]. In the present study, ReO_x NPs were synthesized by the aqueous-phase reduction of NH_4ReO_4 with $NaBH_4$ using HSA as both surface stabilizer as well as coating agent. HSA is a well-known major protein in human plasma and is an excellent candidate for NPs coating to provide enhanced biocompatibility, prolonged blood circulation, and can possibly resolve the issues related to drug-resistance in cancer patients [25]. In fact, several HSA-based drug formulations have been approved for clinical trials and marketed worldwide [29, 58]. Therefore, synthesis of ReO_x NPs coated with HSA opens the doorway for multifunctional and bioinspired nanomaterial for use in cancer theranostics.

Interestingly, under the realms of nuclear medicine, Re based nanoplatforms hold particular significance due to the availability of two theranostic rhenium radioisotopes of particular relevance: ^{186}Re ($T_{½}$ = 90.64 h; $E_{βmax}$ = 1.1 MeV, $E_γ$ = 137 keV) and ^{188}Re ($T_{½}$ = 16.9 h; $E_{βmax}$ = 2.12 MeV, $E_γ$ = 155 keV) [59, 60]. The fusion of these theranostic radiometals with nanotechnology heralds a transformative era in cancer management, promising specific and tailored diagnosis and therapy. Among these two radioisotopes, ^{188}Re is more widely used in nuclear medicine clinics because of its convenient availability as and when required from column chromatographic ^{188}W/^{188}Re generator based on alumina matrix [59]. However, the production of ^{188}W involves double neutron capture reaction on enriched ^{186}W target and can only be achieved with moderate specific activity [61]. Presently, production of ^{188}W is reliant on very few high flux reactors ($\varphi \sim 10^{15}$ n.cm^{-2}.s^{-1}) available in the world and therefore the generators are available commercially at an exorbitant cost which restricts the widespread utilization of this otherwise excellent radioisotope [61]. In the present study, we have utilized an indigenously developed ^{188}W/^{188}Re generator wherein the parent ^{188}W was produced by long-term (6 months) neutron irradiation in a medium flux research

reactor [59]. A high-capacity adsorbent (mesoporous alumina) was used as the column matrix in the generator to mitigate the issues related to low specific activity of the parent radioisotope. The generator demonstrated high elution yields over a prolonged period of 6 months and ^{188}Re could be obtained with adequate purity for use in nuclear medicine applications.

Integration of ^{188}Re in the inorganic nanoplatform (a process known as 'radiolabeling') epitomizes a new class of agents with tremendous potential for clinical applications in nuclear medicine and molecular imaging. Primarily, four different methods are used for radiolabeling nanomaterials for use in cancer imaging and therapy: (a) use of exogeneous chelators for binding with radioisotopes, (b) bombardment of pre-synthesized NPs with hadronic projectiles, (c) physical or chemical adsorption of radioisotopes on the surface of NPs and (d) synthesis of NPs directly using radioactive and non-radioactive precursors [62]. The fourth method also known as "instrinsic" radiolabeling of NPs is gaining particular importance because in this procedure, the radioisotope is a part of the nanocrystal matrix and hence demonstrates excellent radiochemical stability in vivo and thus negligible off-targeting would be exhibited [62]. Moreover, the inherent biological properties of the nanoplatform are not compromised due to minimal surface modification required for loading of radioisotopes in the same. In this study, intrinsically radiolabeled [^{188}Re]ReO_x-HSA NPs could be synthesized with excellent colloidal and radiochemical stability, as evident from the extensive characterization studies.

The emerging concept of multimodality imaging which is based on the strengths of two or more molecular imaging modalities, can provide complete structural, functional and molecular information in a living subject [63]. This is turn offers the scope of better-quality diagnostic and therapeutic monitoring capabilities and greatly accelerates the development of radiolabeled NPs based multimodal molecular imaging [63]. Especially, from this perspective, CT imaging helps to understand the lesions depiction more accurately, while, SPECT/PET imaging intensity correlates well with the pathological changes. Therefore, biocompatible [^{188}Re]ReO_x-HSA NPs bearing intrinsic SPECT and CT imaging properties would afford accurate and precise real-time assessment of biological signatures in cancer patients and thus pave the path towards personalized cancer treatment. To demonstrate the CT enhanced imaging ability of ReO_x-HSA NPs, a CT imaging experiment in vivo was performed. The tumor contrast could be obviously detected after intratumoral administration of ReO_x-HSA NPs while no tumor signal was found before injection under the same conditions, indicating the excellent contrast ability of this nanoagent. Further, in vivo SPECT/CT imaging after intratumoral injection of [^{188}Re]ReO_x-HSA NPs demonstrate selective localization of the radiolabeled agent at the tumor site with minimal leakage to non-targeted organs. This was further corroborated by biodistribution studies. As evident from the autoradiography studies, the radiolabeled NPs distributed homogeneously at the tumor site. These studies established the potential of this radiolabeled nanoplatform for cancer imaging and therapy.

Combination therapy using functionalized nanoplatforms demonstrate intriguing pharmacological control, particularly from the outlook of tailoring personalized cancer treatments with maximized therapeutic synergy for individual patients [64]. In the present study, we have demonstrated the applicability of intrinsically radiolabeled [^{188}Re]ReO_x-HSA NPs for RT, PTT and combined RT/PTT in preclinical settings. Before investigating the potential of [^{188}Re]ReO_x-HSA NPs for combination (RT/PTT) therapy in vivo, excellent cell biocompatibility of ReO_x-HSA NPs was established in B16F10 cell line. On incubation of B16F10 cells with [^{188}Re]ReO_x-HSA NPs and convergence with PTT, cell viability could be inhibited more effectively compared to RT or PTT alone. After establishing the remarkably enhanced killing effect of RT/PTT on cancer cells, we evaluated RT, PTT, and combined RT/PTT for in vivo treatment of melanoma (B16F10) tumor in mice model. It was demonstrated that all three therapies were effective in delaying the tumor growth in mice and that combined RT/PTT was most effective in terms of requirement of relatively lower radioactive dose to reduce side effects. An overview of NPs based combination therapies reported based on preclinical studies over the last decade is given in Table S4 (Supplementary information). Each study utilizes distinct cancer cell lines and tumor models, creating significant variability in experimental conditions. This heterogeneity complicates direct comparisons between these studies, as differences in biological contexts and methodologies can influence outcomes. Based on these studies, it is difficult to draw definitive conclusions about the supremacy of one therapeutic modality over another.

Though notable synergistic treatment effects of [^{188}Re]ReO_x-HSA NPs have been observed and also numerically established by Valeriote's method [45], the underlying detailed mechanisms and the response of the pathological environment to combined RT/PTT need to be further explored. Additionally, long-term toxicity and survival studies are warranted to determine the optimal dose and fractionation schedule for the treatment strategy. This in turn would be a meaningful guide towards clinical translation of such intrusive study for cancer treatment. Another main challenge associated with this class of NPs is that they can effectively treat primary tumors but do not target metastases. To overcome this limitation, incorporating specific targeting ligands onto the NPs can improve their ability to identify and attach to metastatic sites. Nevertheless, in view of

the promising results obtained in the present study, [^{188}Re]ReO_x-HSA NPs have high potential as biocompatible and biodegradable metallic theranostic agent for SPECT/CT imaging guided combined RT/PTT of cancer.

Conclusion

In summary, we have synthesized biocompatible, intrinsically radiolabeled [^{188}Re]ReO_x NPs stabilized by HSA and demonstrated their efficacy towards cancer theranostics in preclinical settings. The utilization of biocompatible HSA precluded the use of toxic chemicals which are commonly used for enhancing the colloidal stability in nanoformulations. The synthesized NPs could be used for dual modality (SPECT/CT) imaging of tumor. Also, [^{188}Re]ReO_x - HSA NPs could be used for combined RT/PTT and it was demonstrated that this synergistic approach was more effective to arrest the tumor growth in mice model compared to individual modalities (RT or PTT) alone. Moreover, the effect of combination therapy did not lead to serious toxicity concerns as evident from the hematological and biochemical parameters of the treated mice and also histopathology studies. The unique features of [^{188}Re]ReO_x -HSA NPs providing the scope for both SPECT/CT imaging as well as concurrent RT/PTT promising the potential for clinical translation of this theranostic nanomedicine in foreseeable future. This strategy would not only personalize the treatment protocol but also improve the therapeutic outcomes over traditional RT using radiopharmaceuticals since it is able to ablate tumor with relatively lower radioactive doses in order to minimize the side effects of treatment in cancer patients.

Supplementary Information The online version contains supplementary material available at https://doi.org/10.1007/s00259-025-07074-9.

Acknowledgements The authors are thankful to Dr. Y. K. Bhardwaj, Associate Director, Radiochemistry and Isotope Group, Bhabha Atomic Research Centre (BARC), Dr. Sandip Basu, Head, Radiation Medicine Centre (Medical), BARC, Dr. Tapas Das, Head, Radiopharmaceuticals Division (RPhD), BARC and Dr. Sudipta Chakraborty, Head, Radiochemicals Section, RPhD, BARC for their support to this work. Dr. A.K. Debnath, Technical Physics Division, BARC, is acknowledged for providing the XPS data. Dr. Manisha Banerjee, Molecular Biology Division, BARC is acknowledged for providing the circular dichroism data. Thanks are due to Mr. Ramu Ram of RPhD, BARC for participtaing in the radiochemical processing of irradiated tungsten target for preparation of the ^{188}W/^{188}Re generator. Mr. Renjith B. Nelliyil, Radiochemistry Division, BARC is gratefully acknowledged for providing XRD data. The Sophisticated Analytical Instrumentation Facility of the Indian Institute of Technology Bombay, Mumbai is gratefully acknowledged for the TEM/HRTEM analyses of the samples.

Author contributions Sanchita Ghosh: Data curation, Formal analysis, Writing - original draft preparation; Apurav Guleria: Data curation, Formal analysis; Sourav Patra: Data curation; Avik Chakraborty: Data curation, Formal analysis; Kanhu Charan Barick: Data curation, Formal analysis; Chandan Kumar: Data curation; Khajan Singh: Data curation; Sutapa Rakshit: Data curation; Rubel Chakravarty: Conceptualization, Data curation, Formal analysis, Investigation, Project administration, Supervision, Writing – original draft, Writing – review & editing.

Funding Open access funding provided by Department of Atomic Energy.
This work was supported by internal funding received from the Bhabha Atomic Research Centre, Mumbai, India.

Data availability All data generated or analyzed during this study are included in this published article and its supplementary information files.

Declarations

Ethics approval All animal studies were performed according to the guidelines of the Animal Care and Use Committee of the Bhabha Atomic Research Centre, India.

Consent to publish All authors have read this manuscript and would like to have it considered for publication.

Conflicts of interest All authors declare that they have no conflict of interest.

References

1. Bray F, Laversanne M, Sung H, Ferlay J, Siegel RL, Soerjomataram I, et al. Global cancer statistics 2022: GLOBOCAN estimates of incidence and mortality worldwide for 36 cancers in 185 countries. CA Cancer J Clin. 2024;74:229–63.
2. Da J, Di X, Xie Y, Li J, Zhang L, Liu Y. Recent advances in nanomedicine for metabolism-targeted cancer therapy. Chem Commun (Camb). 2024;60:2442–61.
3. Fan D, Cao Y, Cao M, Wang Y, Cao Y, Gong T. Nanomedicine in cancer therapy. Signal Transduct Target Ther. 2023;8:293.
4. Ji B, Wei M, Yang B. Recent advances in nanomedicines for photodynamic therapy (PDT)-driven cancer immunotherapy. Theranostics. 2022;12:434–58.

5. Wei G, Wang Y, Yang G, Wang Y, Ju R. Recent progress in nanomedicine for enhanced cancer chemotherapy. Theranostics. 2021;11:6370–92.
6. Yu S, Chen Z, Zeng X, Chen X, Gu Z. Advances in nanomedicine for cancer starvation therapy. Theranostics. 2019;9:8026–47.
7. Yook S, Cai Z, Lu Y, Winnik MA, Pignol J-P, Reilly RM. Intratumorally injected ^{177}Lu-labeled gold nanoparticles: gold nanoseed brachytherapy with application for neoadjuvant treatment of locally advanced breast cancer. J Nucl Med. 2016;57:936–42.
8. Kim JS, Rieter WJ, Taylor KM, An H, Lin W, Lin W. Self-assembled hybrid nanoparticles for cancer-specific multimodal imaging. J Am Chem Soc. 2007;129:8962–3.
9. Gavas S, Quazi S, Karpiński TM. Nanoparticles for cancer therapy: current progress and challenges. Nanoscale Res Lett. 2021;16:173.
10. Chen Z, Wan L, Yuan Y, Kuang Y, Xu X, Liao T, et al. pH/GSH-dual-sensitive hollow mesoporous silica nanoparticle-based drug delivery system for targeted cancer therapy. ACS Biomater Sci Eng. 2020;6:3375–87.
11. Dang Y, Guan J. Nanoparticle-based drug delivery systems for cancer therapy. Smart Mater Med. 2020;1:10–9.
12. Scicluna MC, Vella-Zarb L. Evolution of nanocarrier drug-delivery systems and recent advancements in covalent organic framework–drug systems. ACS Appl Nano Mater. 2020;3:3097–115.
13. Shen B, Ma Y, Yu S, Ji C. Smart multifunctional magnetic nanoparticle-based drug delivery system for cancer thermo-chemotherapy and intracellular imaging. ACS Appl Mater Interfaces. 2016;8:24502–8.
14. Bajpai S, Tiwary SK, Sonker M, Joshi A, Gupta V, Kumar Y, et al. Recent advances in nanoparticle-based cancer treatment: a review. ACS Appl Nano Mater. 2021;4:6441–70.
15. Zhao M, van Straten D, Broekman ML, Préat V, Schiffelers RM. Nanocarrier-based drug combination therapy for glioblastoma. Theranostics. 2020;10:1355.
16. Cheng D, Gong J, Wang P, Zhu J, Yu N, Zhao J, et al. 131 I-Labeled gold nanoframeworks for radiotherapy-combined second near-infrared photothermal therapy of cancer. J Mater Chem B. 2021;9:9316–23.
17. Zhang C, Chai J, Jia Q, Tan J, Meng Z, Li N, et al. Evaluating the therapeutic efficacy of radiolabeled BSA@ CuS nanoparticle-induced radio-photothermal therapy against anaplastic thyroid cancer. IUBMB Life. 2022;74:433–45.
18. Ferreira CA, Ni D, Rosenkrans ZT, Cai W. Radionuclide-activated nanomaterials and their Biomedical Applications. Angew Chem Int Ed Engl. 2019;58:13232–52.
19. Ferreira CA, Ehlerding EB, Rosenkrans ZT, Jiang D, Sun T, Aluicio-Sarduy E, et al. $^{86/90}$Y-LamonoclonalcantibodyttargetingtissueTfactorFactopancreaticrcancerCtheranosticsostics. Mol Pharm. 2020;17:1697–705.
20. Tanaka T, Akahane T, Bannai E, Kawai S, Tsuda N, Ishizawa Y. Role of polar optical phonon scattering in electrical resistivities of LaB_6 and ReO_3. J Phys C: Solid State Phys. 1976;9:1235–41.
21. Allen PB, Schulz WW. Bloch-Boltzmann analysis of electrical transport in intermetallic compounds: ReO_3, $BaPbO_3$, $CoSi_2$, and Pd_2Si. Phys Rev B Condens Matter. 1993;47:14434–9.
22. Biswas K, Rao CN. Metallic ReO_3 nanoparticles. J Phys Chem B. 2006;110:842–5.
23. Wang X, Wang J, Pan J, Zhao F, Kan D, Cheng R, et al. Rhenium Sulfide nanoparticles as a Biosafe Spectral CT Contrast Agent for Gastrointestinal Tract Imaging and tumor theranostics in vivo. ACS Appl Mater Interfaces. 2019;11:33650–8.
24. Kleynhans J, Duatti A, Bolzati C. Fundamentals of rhenium-188 radiopharmaceutical chemistry. Molecules. 2023;28:1487.
25. Chakravarty R, Guleria A, Jadhav S, Kumar C, Debnath AK, Sarma HD, et al. Bioinspired synthesis of intrinsically ^{177}Lu-labeled hybrid nanoparticles for potential cancer therapy. Ind Eng Chem Res. 2020;59:22492–500.
26. Ghosh S, Patra S, Younis MH, Chakraborty A, Guleria A, Gupta SK, et al. Brachytherapy at the nanoscale with protein functionalized and intrinsically radiolabeled [^{169}Yb] Yb_2O_3 nanoseeds. Eur J Nucl Med Mol Imaging. 2024;15:1558–1573.
27. Zhang X, Chen F, Turker MZ, Ma K, Zanzonico P, Gallazzi F, et al. Targeted melanoma radiotherapy using ultrasmall ^{177}Lu-labeled α-melanocyte stimulating hormone-functionalized core-shell silica nanoparticles. Biomaterials. 2020;241:119858.
28. Chakravarty R, Shetty P, Nair KV, Rajeswari A, Jagadeesan K, Sarma HD, et al. Reactor produced [^{64}Cu]$CuCl_2$ as a PET radiopharmaceutical for cancer imaging: from radiochemistry laboratory to nuclear medicine clinic. Ann Nucl Med. 2020;34:899–910.
29. Tongkanarak K, Loupiac C, Neiers F, Chambin O, Srichana T. Evaluating the biomolecular interaction between delamanid/formulations and human serum albumin by fluorescence, CD spectroscopy and SPR: effects on protein conformation, kinetic and thermodynamic parameters. Colloids Surf B Biointerfaces. 2024;239:113964.
30. Nudelman R, Alhmoud H, Delalat B, Kaur I, Vitkin A, Bourgeois L, et al. From nanoparticles to crystals: one-pot programmable biosynthesis of photothermal gold structures and their use for biomedical applications. J Nanobiotechnol. 2022;20:482.
31. Das L, Guleria A, Adhikari S. Aqueous phase one-pot green synthesis of SnSe nanosheets in a protein matrix: negligible cytotoxicity and room temperature emission in the visible region. RSC Adv. 2015;5:61390–7.
32. Anantharaj S, Sakthikumar K, Elangovan A, Ravi G, Karthik T, Kundu S. Ultra-small rhenium nanoparticles immobilized on DNA scaffolds: an excellent material for surface enhanced Raman scattering and catalysis studies. J Colloid Interface Sci. 2016;483:360–73.
33. Dingari NC, Horowitz GL, Kang JW, Dasari RR, Barman I. Raman spectroscopy provides a powerful diagnostic tool for accurate determination of albumin glycation. PLoS ONE. 2012;7:e32406.
34. Rygula A, Majzner K, Marzec KM, Kaczor A, Pilarczyk M, Baranska M. Raman spectroscopy of proteins: a review. J Raman Spectrosc. 2013;44:1061–76.
35. Szekeres GP, Kneipp J. Different binding sites of serum albumins in the protein corona of gold nanoparticles. Analyst. 2018;143:6061–8.
36. Li M-M, Cao J-W, Qin X-L, Liu X-Y, Yuan X-Q, Dong X-T, et al. Theoretical prediction of Rhenium separation from ammonium perrhenate by phonon–photon resonance absorption. ACS Omega. 2022;7:5437–41.
37. Agullo-Rueda F, Calleja J, Bartolome J. Raman spectroscopy of the ammonium ion in NH_4MnF_3 and NH_4ZnF_3 perovskites: temperature dependence. J Phys C: Solid State Phys. 1988;21:1287.
38. Korppi-Tommola J, Devarajan V, Brown R, Shurvell H. The temperature dependence of the Raman spectrum of ammonium perrhenate. J Raman Spectrosc. 1978;7:96–100.
39. Bazuev G, Chupakhina T, Korolyov A, Kuznetsov M. Synthesis under usual conditions, X-ray photoelectron spectroscopy and magnetic properties of $Re_{1-x}Mn_xO_2$ oxides with rutile structure. Mater Chem Phys. 2010;124:946–51.
40. Shim J, Oh A, Kang DH, Oh S, Jang SK, Jeon J, et al. High-performance 2D rhenium disulfide (ReS_2) transistors and photodetectors by oxygen plasma treatment. Adv Mater. 2016;28:6985–92.
41. Tysoe W, Zaera F, Somorjai G. An XPS study of the oxidation and reduction of the rhenium-platinum system under atmospheric conditions. Surf Sci. 1988;200:1–14.
42. Yuan Y, Shido T, Iwasawa Y. The new catalytic property of supported rhenium oxides for selective oxidation of methanol to methylal. Chem comm. 2000;15:1421–22.

43. Okal J, Tylus W, Kępiński L. XPS study of oxidation of rhenium metal on γ-Al_2O_3 support. J Catal. 2004;225:498–509.
44. Pawlak DA, Ito M, Oku M, Shimamura K, Fukuda T. Interpretation of XPS O (1s) in mixed oxides proved on mixed perovskite crystals. J Phys Chem B. 2002;106:504–7.
45. Deinavizadeh M, Kiasat AR, Shafiei M, Sabaeian M, Mirzajani R, Zahraei SM, et al. Synergistic chemo-photothermal therapy using gold nanorods supported on thiol-functionalized mesoporous silica for lung cancer treatment. Sci Rep. 2024;14:4373.
46. De La Vega JC, Esquinas PL, Gill JK, Jessa S, Gill B, Thakur Y, et al. Comparison of Rhenium and Iodine as contrast agents in X-Ray imaging. CMMI. 2021;2021:1250360.
47. Aslan N, Ceylan B, Koç MM, Findik F. Metallic nanoparticles as X-Ray computed tomography (CT) contrast agents: a review. J Mol Struct. 2020;1219:128599.
48. Hasebroock KM, Serkova NJ. Toxicity of MRI and CT contrast agents. Expert Opin Drug Metab Toxicol. 2009;5:403–16.
49. Chen F, Ehlerding EB, Cai W. Theranostic nanoparticles. J Nucl Med. 2014;55:1919–22.
50. Chakravarty R, Goel S, Dash A, Cai W. Radiolabeled inorganic nanoparticles for positron emission tomography imaging of cancer: an overview. Q J Nucl Med Mol Imaging. 2017;61:181–204.
51. Ge J, Chen L, Huang B, Gao Y, Zhou D, Zhou Y, et al. Anchoring group-mediated radiolabeling of inorganic nanoparticles a universal method for constructing nuclear medicine imaging nanoprobes. ACS Appl Mater Interfaces. 2022;14:8838–46.
52. Zhang W, Deng G, Li B, Zhao X, Ji T, Song G, et al. Degradable rhenium trioxide nanocubes with high localized surface plasmon resonance absorbance like gold for photothermal theranostics. Biomaterials. 2018;159:68–81.
53. Belyaev IB, Zelepukin IV, Kotelnikova PA, Tikhonowski GV, Popov AA, Kapitannikova AY, et al. Laser-synthesized germanium nanoparticles as biodegradable material for Near-Infrared Photoacoustic Imaging and Cancer Phototherapy. Adv Sci. 2024;11:2307060.
54. Na H, Carrier J, Oyon S, Lai CY. Fabrication of Rhenium Disulfide/Mesoporous Silica Core-Shell Nanoparticles for a pH-Responsive drug release and combined chemo-photothermal therapy. ACS Appl Bio Mater. 2024;7:3337–45.
55. Hu S, Hamilton SG, Turner CL, Robertson DD, Yan J, Kavner A, et al. High-pressure studies of size dependent yield strength in rhenium diboride nanocrystals. Nanoscale Horiz. 2024;9:646–55.
56. Murugan SS, Hur W, Son SE, Lee HB, Ha CH, Lee SJ, et al. The therapeutic efficacy of silver loaded rhenium disulfide nanoparticles as a photothermal agent for cancer eradication. J Photochem Photobiol B. 2024;250:112831.
57. Na H, Venedicto M, Chang CY, Carrier J, Lai CY. Infrared-activated bactericide: Rhenium Disulfide (ReS_2)-Functionalized mesoporous silica nanoparticles. ACS Appl Bio Mater. 2023;6:1577–85.
58. Shastri D, Raj V, Lee S. Revolutionizing Alzheimer's treatment: harnessing human serum albumin for targeted drug delivery and therapy advancements. Ageing Res Rev. 2024;99:102379.
59. Chakravarty R, Bahadur J, Lohar S, Jadhav S, Sen D, Chakraborty S. Mechanochemically synthesized mesoporous alumina: a smart new-generation sorbent for preparation of chromatographic $^{188}W/^{188}Re$ generator. SN Appl Sci. 2021;3:1–9.
60. Ram R, Chakravarty R, Jadhav S, Chakraborty S, Jagadeesan K, Thakare S, et al. Radiochemical separation of no-carrier-added ^{186}Re from proton irradiated tungsten target. J Radioanal Nucl Chem. 2020;325:875–83.
61. Chakravarty R, Shukla R, Ram R, Venkatesh M, Tyagi AK, Dash A. Exploitation of nano alumina for the chromatographic separation of clinical grade ^{188}Re from ^{188}W: a renaissance of the $^{188}W/^{188}Re$ generator technology. Anal Chem. 2011;83:6342–8.
62. Ghosh S, Lee SJ, Hsu JC, Chakraborty S, Chakravarty R, Cai W. Cancer Brachytherapy at the Nanoscale: an emerging paradigm. Chem Biomed Imaging. 2023;2:4–26.
63. Calatayud DG, Lledos M, Casarsa F, Pascu SI. Functional diversity in Radiolabeled Nanoceramics and related biomaterials for the Multimodal Imaging of Tumors. ACS Bio Med Chem Au. 2023;3:389–417.
64. Labrie M, Brugge JS, Mills GB, Zervantonakis IK. Therapy resistance: opportunities created by adaptive responses to targeted therapies in cancer. Nat Rev Cancer. 2022;22:323–39.